Sensorless Generalized Average Modeling-Based Control for the Resonant LC-DAB Converter

Original Scientific Paper

Adelina Mukhametdinova
Shanghai Jiao Tong University, School of Electronics Information and Electrical Engineering
800 Dongchuan Rd, Shanghai, China
adelinam@sjtu.edu.cn

Muhammad Mansoor Khan*
Shanghai Jiao Tong University, School of Electronics Information and Electrical Engineering
800 Dongchuan Rd, Shanghai, China
mansoor@sjtu.edu.cn

Ruifeng Zhang
Shanghai Jiao Tong University, School of Electronics Information and Electrical Engineering
800 Dongchuan Rd, Shanghai, China
zrf333@sjtu.edu.cn

*Corresponding author

Abstract *– The dual active bridge (DAB) converter is an efficient power conversion topology designed for applications that require bidirectional galvanic isolation and energy transfer. Among its various configurations, the resonant LC-DAB converter is notable for its ability to significantly reduce switching losses and enhance efficiency. While discrete-time control methodologies are widely employed for design and analysis of DAB converters, it is challenging to ensure performance stability during steady-state and transient operating modes. Furthermore, high-frequency and single point measurement of resonant LC-DAB possess challenge, as it may not reflect the behavior of resonant inductor current. To address these issues, a generalized average modeling-based approach is proposed, which minimizes output-side circulating current. This is achieved by aligning the output current with the secondary side converter's voltage. The proposed model eliminates the need for a current sensor and demonstrates low sensitivity during transient conditions. A two-stage control loop is utilized: an inner loop for current control and an outer loop with a PI controller for voltage control. The analysis and design procedure for the proposed control is detailed, followed by simulation and experimental results in order to demonstrate the effectiveness of the proposed method.*

Keywords: *Dual active bridge, resonant DC-DC converter, generalized average modelling, sensorless control*

Received: October 25, 2024; Received in revised form: January 6, 2025; Accepted: January 19, 2025

1. INTRODUCTION

The DC-DC converter is essential as an interface between different DC-bus levels. It has been utilized in many applications, such as automotive applications [1], PV applications [2], DC transmission systems [3], and DC microgrids [4]. DAB DC-DC converter offers the advantages of a high step-down conversion ratio, high power transfer efficiency, bidirectional power flow, and galvanic isolation between the input and output stages [5-7]. The mode in which the converter operates with the current aligned with the secondary side voltage is preferred in many power electronics converters, as it minimizes switching losses [8]-[10]. In this mode, the current through the inductor returns to zero at the end of each switching cycle, but it does not stay at zero for a long period. One of the main challenges in power conversion systems is handling fluctuations in input voltage and varying load operations. These factors can lead to output voltage ripple and instability in the DAB system [11-13]. To solve this problem, a control loop can be used to ensure stability and maintain dynamic performance. However, measuring high-frequency current poses a challenge. Various authors in the existing

literature have proposed different methods for current measurement, including direct and indirect measurement of current, and current sensorless control.

The first category for current measurement uses a high-frequency current sensor to measure the current in real-time. This approach was employed in a robust digital nonlinear control system based on asymmetric half-cycle modulation [14]. It features model-based predictive current control with a compensator using a geometric sequence-control algorithm. This system demonstrates a smooth transient response, but its practical application is limited due to the requirement of a high-bandwidth current sensor. Another approach, a digital predictive controller for single-phase shift modulation, is proposed in [15-17]. The controller tracks the current reference within a single switching cycle to ensure that the transient DC offset is removed from the transformer current. It provides inherent over-current protection for the transformer but requires midpoint current sampling, leading to design complexity.

The second category involves indirect current measurement. In [18], the voltage across the extra input resistor is used for a feedforward controller. It measures the DAB converter's average input current under single phase shift modulation by analog integrator. Although this method shows a good dynamic response, however it requires additional complicated hardware. Another technique uses a load-current estimating method under a single-phase shift with switching-period delay compensation [19]. This method estimates the load current by measuring input and output voltage differences. The measurement noise is reduced by adopting the damping coefficient. However, this method increases the control complexity due to the load current estimating and input voltage sampling processes.

In the third category, current-sensorless control, eliminates the need for a current sensor. A model predictive control scheme under dual phase shift modulation without a current sensor can predict the output power in the following switching cycle [20]. It uses the deviation between the reference voltage and input voltage. This method has low hardware cost and good dynamic performance. However, a sampling delay makes the feedback loop time constant large. Another paper proposes a current sensor-reduction control with an extended state observer under dual-phase-shift modulation [21]. The observed load current is directly used to predict phase-shift duty ratios after each switching cycle. This results in cost savings and increased reliability. Additionally, the proposed method can eliminate the steady-state error of the output voltage. However, the observer's accuracy depends on the precision of the model parameters.

Table 1 presents a comparative summary of various current measurement techniques, highlighting their respective advantages and limitations. Direct current measurement can be accurate but has high cost and limited practical application. In contrast, indirect current measurement tends to have a lower cost but may have implementation complexity. Sensorless current control offer elimination of sensors, which can reduce costs and simplify system design. Nevertheless, they often suffer from issues of accuracy.

Conventional converters typically utilize a pure inductor for damping purposes. These converters offer simplicity in analysis but have high switching and RMS urrents, reducing efficiency [22, 23]. In contrast, the resonant DAB converter incorporates an inductor in series with a capacitor, forming a resonant tank that acts as the power impedance. This decreases the peak current and the transformer current's DC component, which enhances efficiency [24, 25]. However, its dynamic behavior can introduce significant stability challenges, necessitating the development of control strategies to mitigate oscillations and maintain performance across various operating conditions.

Table 1. Current measurement techniques comparison

Current measurement method	Controller type	Modulation technique	Benefit	Drawback	Reference
Direct measurement	Robust digital nonlinear control	Asymmetric half-cycle modulation	Smooth transient response	Limited practical application	[14]
Direct measurement	Digital predictive controller	Single phase shift	Inherent overcurrent protection ability	Midpoint current sampling requirement, high cost	[15]-[17]
Indirect current measurement	Feedforward controller	Single phase shift	Good dynamic response	Additional complicated hardware requirement	[18]
Indirect current measurement	Load-current estimating method	Single phase shift	Low measurement noise	Control complexity	[19]
Sensorless current control	Model predictive control	Dual phase shift	Low hardware cost and good dynamic performance	Large feedback loop time, inaccuracy	[20]
Sensorless current control	Sensor-reduction control with an extended state observer	Dual phase shift	Low-cost, good reliability, elimination of output voltage steady-state error	Accuracy dependence on the model parameters	[21]

Different works performed control strategies for resonant DAB converters. The paper [26] discusses phase shift compensation with unified boundary control for resonant LC-DAB based on triple-phase-shift modula-

tion. It presents a steady-state analysis utilizing various modulation controls to minimize circulating current and enhance converter efficiency. However, it can work only at frequencies much higher than resonant frequency which may tend to higher switching losses. Another method uses frequency-domain analysis, representing current and voltage waveforms in a high-frequency link form [27]. This method accommodates variables related to multiple phase shifts. It can guarantee soft-switching operation, while minimizing the reactive power circulating between the bridges. However, it requires complex calculations to minimize reactive circulating power. The authors in [28] develop a small-signal model by extending the description function to predict the low-frequency behavior of the resonant LC-DAB. The model investigates the effects of switching frequency and phase shift as control parameters, incorporating a compensator into the control loop to enhance the dynamic response of resonant converters. However, accurately detecting both phase and gain relationships incurs high hardware costs and significant computational time.

Additionally, previous research primarily focused on adjusting the duty cycle, which becomes less effective when operating near the resonant frequency. These methods typically require the switching frequency to be at least 20% higher than the resonant frequency in order to function correctly [29]. Furthermore, it is observed that a significant portion of the existing literature has primarily employed discrete-time steady-state models, which can complicate the analysis and evaluation of a system's overall effectiveness. In contrast, using a continuous-time model facilitates a more straightforward evaluation of system behavior. The resonant LC-DAB model can be obtained through generalized average modeling (GAM) which provides continuous-time representations of AC state variables by utilizing complex Fourier coefficients [30, 31]. This approach provides a balanced trade-off between complexity and accuracy, enabling the ability of both zero current switching and zero voltage switching.

By considering the limitations discussed in prior research, the key contributions of this study, therefore are:

1. The GAM-based control has been proposed to effectively minimize circulating current on the output side by ensuring that the output current phase is aligned with the voltage of the secondary side converter.
2. By aligning the output current with the voltage, the model significantly reduces the current during switching, which enhances overall converter efficiency.
3. The model uses a sensorless control approach with continuous time representation. It allows for a more straightforward assessment of system behavior under varying conditions, eliminating the need for physical sensors that can introduce complexity and potential points of failure. The model has been verified through analysis and simulation.

The remainder of this paper is organized as follows. Section 2 presents the operation principle and GAM analysis of the resonant LC-DAB converter. Section 3 details the proposed control methodology, including inner and outer loop control. Section 4 presents the simulation and experimental results in detail with a comparison of the previous discussed method and proposed method. Finally, Section 5 concludes the paper.

2. STRUCTURE AND BASICS OF PROPOSED CONVERTER SYSTEM

2.1. CONVERTER TOPOLOGY

Fig. 1 shows a schematic of a resonant DAB converter. It consists of two full bridges on the primary and secondary sides, resonant inductance L, resonant capacitor C, and a high-frequency transformer characterized by a turn's ratio n. The full bridges consist of eight MOSFETs S1–S8 with antiparallel diodes D1–D8. The terms Ci, C_o, R_o, are the input, output capacitors, output resistance respectively. V_{in}, V_{out}, i_{out}, v_{AB}, v_{CD}, i_r, v_{LC} are input voltage, output voltage, output current, primary side voltage, secondary side voltage, inductor current, and LC-tank voltage, respectively.

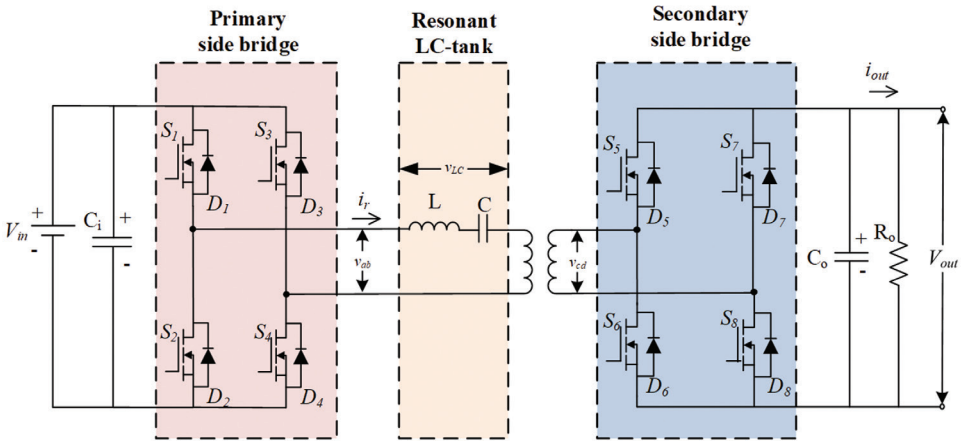

Fig. 1. Single-stage resonant LC-DAB

Fig. 2 illustrates the operating waveforms of resonant LC-DAB with output-aligned current. In stages 1 and 2, the inductor current is positive, conversely, in stages 3 and 4, the inductor current is negative. At time t_2, the current approaches zero, allowing for ZCS to be achieved which leads to reduced switching losses. The normalized phase shift between leading and lagging leg of primary side is defined as d. The fundamental harmonic approximation is indicated by the dashed line. Notably, the phase shift between the resonant current and the first harmonic voltage of the secondary side is zero, while the phase shift between the resonant current and the first harmonic voltage of the primary side is represented as φ for illustration purpose. Both the duty cycle d and phase shift φ in a real implementation are smaller than those illustrated in the graph; however, they have been exaggerated for clearer understanding.

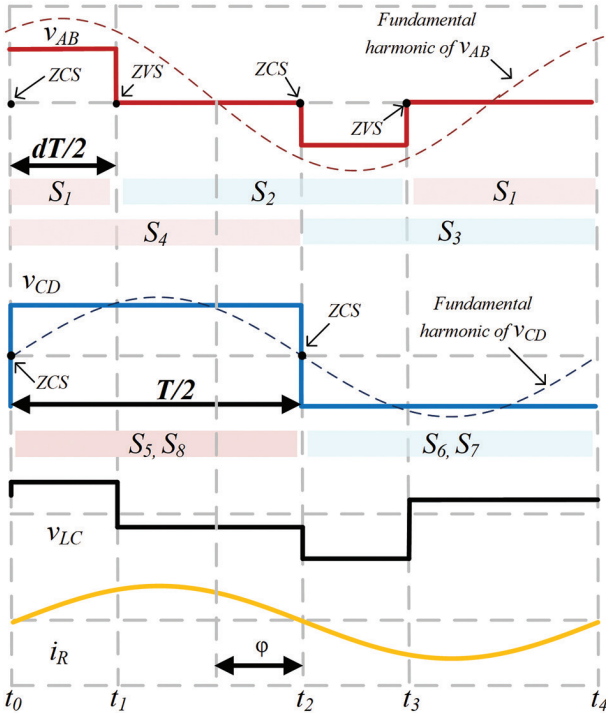

Fig. 2. Operating waveforms of the resonant LC-DAB

2.2. GENERALIZED AVERAGE MODELING

The GAM can formulate linear and time-invariant state equations. Throughout the analysis, τ represents the time referenced to the rising edge of s_1. State variable $z(t)$ during the interval $t - T \le \tau \le$ can be expressed using Fourier series expansion as follows [30]:

$$z(t) = \sum_{k=-\infty}^{+\infty} \langle z \rangle_k (t) e^{jk\omega t}, \tag{1}$$

Where $\omega = 2\pi f_s$, $\langle z \rangle_k$ - coefficient of the kth harmonics, which is defined by

$$\langle z \rangle_k (t) = \frac{1}{T} \int_{t-T}^{t} z(\tau) e^{-jk\omega\tau} d\tau. \tag{2}$$

The transformer current is entirely AC in a DAB converter, resulting in a significant ripple and a zero DC component. To accurately represent the state variable averages in DAB converters, it is necessary to include multiple terms ($k = 0$ and $k = \pm 1$) in the Fourier expansion.

The product of 0th-order coefficient terms is

$$\langle mn \rangle_0 = \langle m \rangle_0 \langle n \rangle_0 + 2(\langle m \rangle_{1R} \langle n \rangle_{1R} + \langle m \rangle_{1I} \langle n \rangle_{1I}). \tag{3}$$

The 1st-order coefficient terms of two terms are

$$\langle mn \rangle_{1R} = \langle m \rangle_0 \langle n \rangle_{1R} + \langle m \rangle_{1R} \langle n \rangle_0, \tag{4}$$

$$\langle mn \rangle_{1I} = \langle m \rangle_0 \langle n \rangle_{1I} + \langle m \rangle_{1I} \langle n \rangle_0. \tag{5}$$

Where the lower indexes "R" and "I" represent the real and the imaginary parts of a complex number, respectively.

According to the graph in Fig. 2, the phase shift between the primary and secondary side legs is considered to be equal to zero, with the output voltage aligned with the leading leg of the secondary side. The 0th-order coefficients of and $s_2(\tau)$ are zero due to a fixed 50% duty ratio. The switching function $s_1(\tau)$ of input side voltage has three states (1, 0, -1) and it can be defined as:

$$s_1(\tau) = \begin{cases} 1, 0 \le \tau < \dfrac{dT}{2} \\ 0, \dfrac{dT}{2} \le \tau < \dfrac{T}{2}, \dfrac{dT}{2} + \dfrac{T}{2} \le \tau < T \\ -1, \dfrac{T}{2} \le \tau < \dfrac{dT}{2} + \dfrac{T}{2} \end{cases}. \tag{6}$$

Similarly, the output side switching function $s_2(\tau)$ has two states (1, -1) and can be represented as:

$$s_2(\tau) = \begin{cases} 1, 0 \le \tau < \dfrac{T}{2} \\ -1, \dfrac{T}{2} \le \tau < T \end{cases}. \tag{7}$$

For output-aligned current, the 1st-order coefficients of primary and secondary side switching functions are obtained from the Fourier series expansion of the signal, derived in Eqs. (1)—(3), (6)—(7):

$$\left.\begin{aligned} \langle s_1(\tau) \rangle_{1R} &= \frac{sind\pi}{\pi} \\ \langle s_1(\tau) \rangle_{1I} &= \frac{-1 + cosd\pi}{\pi} \\ \langle s_2(\tau) \rangle_{1R} &= 0 \\ \langle s_2(\tau) \rangle_{1I} &= -\frac{2}{\pi} \end{aligned}\right\}, \tag{8}$$

Using GAM and derived switching function (8), a large signal model for resonant DAB converter can be obtained [31]:

$$\begin{aligned} \frac{d}{dt} \langle i_s(\tau) \rangle_{1R} = {} & \frac{sind_1\pi}{\pi L_r} V_{in} - \frac{R_s}{L_r} \langle i_s(\tau) \rangle_{1R} \\ & - \frac{1}{L_r} \langle v_s(\tau) \rangle_{1R} + 2\pi f_s \langle i_s(\tau) \rangle_{1I}, \end{aligned} \tag{9}$$

$$\begin{aligned} \frac{d}{dt} \langle i_s(\tau) \rangle_{1I} = {} & \frac{-1 + cosd_1\pi}{\pi L_r} V_{in} - \frac{R_s}{L_r} \langle i_s(\tau) \rangle_{1I} \\ & - \frac{1}{L_r} \langle v_s(\tau) \rangle_{1I} + \frac{2}{\pi n L_r} \langle v_0(\tau) \rangle_0 \\ & - 2\pi f_s \langle i_s(\tau) \rangle_{1R}, \end{aligned} \tag{10}$$

$$\frac{d}{d\tau}\left\langle v_0(\tau)\right\rangle_0 = -\frac{1}{C_0 R_o}\left\langle v_0(\tau)\right\rangle_0 - \frac{4}{n\pi C_0}\left\langle i_s(\tau)\right\rangle_{1I}, \quad (11)$$

$$\frac{d}{d\tau}\left\langle v_s(\tau)\right\rangle_{1R} = \frac{1}{C_r}\left\langle i_s(\tau)\right\rangle_{1R} + 2\pi f_s \left\langle v_s(\tau)\right\rangle_{1I}, \quad (12)$$

$$\frac{d}{d\tau}\left\langle v_s(\tau)\right\rangle_{1I} = \frac{1}{C_r}\left\langle i_s(\tau)\right\rangle_{1I} - 2\pi f_s \left\langle v_s(\tau)\right\rangle_{1R}, \quad (13)$$

Where $\langle i_s(\tau)\rangle_{1R}$, $\langle i_s(\tau)\rangle_{1I}$ are the 1st-order of real and imaginary parts of series inductance current; $\langle v_0(\tau)\rangle_0$ is the 0th-order of output voltage; $\langle v_s(\tau)\rangle_{1R}$, $\langle v_s(\tau)\rangle_{1I}$ are the 1st-order real and imaginary parts of resonant capacitor voltage.

The current on the output side can only have two states: 1) the i_{out} when transistors $S6$ and $S7$ are OFF; and 2) the $-i_{out}$ when transistors are $S5$ and $S8$ OFF. Therefore,

$$i_{out}(\tau) = s_2(\tau) i_s(\tau). \quad (14)$$

Only the 0th-order coefficient of output current is considered, as both are DC components. Therefore, by applying Fourier expansion in (3), the 0th-order coefficient of output current can be found:

$$\left\langle i_{out}(\tau)\right\rangle_0 = \left\langle s_2(\tau)\right\rangle_0 \left\langle i_s(\tau)\right\rangle_0 + 2\left(\left\langle s_2(\tau)\right\rangle_{1R} \left\langle i_s(\tau)\right\rangle_{1R}\right. \quad (15)$$

3. PROPOSED CONTROL METHODOLOGY

3.1. OUTPUT-ALIGNED CONTROL METHOD

Existing research employed discrete-time modeling and steady-state analysis for zero voltage switching (ZVS) and zero current switching (ZCS) [17, 32]. However, the solutions derived were overly complex and not directly applicable to microcontrollers. To address this, the researchers made approximations that are only effective at high frequencies. Additionally, the stability and sensitivity of ZVS and ZCS during transients have not been guaranteed or thoroughly analyzed. While these methods may perform well under steady-state conditions, they do not necessarily ensure ZVS and ZCS during transient.

According to (7), the secondary side switching function is aligned with the leading leg, causing the fundamental component to be oriented along the imaginary axis. For optimal performance, the inductive current should mainly consist of an active component with a minimum reactive component, as it does not contribute to energy transfer. To achieve ZVS and ZCS, the inductive current should predominantly feature an imaginary component with a minimized real part.

The duty cycle dcan be calculated differently depending on load conditions in the output-aligned current mode. Nevertheless, the proposed implementation has been approximated using the Taylor approximation [8]:

$$d = \frac{V_{out}}{V_{in}}. \quad (16)$$

I_{ref} is the desired output current value during steady-state for the proposed controller design. Therefore,

$$I_{ref} = -\frac{4}{\pi}\left\langle i_s(\tau)\right\rangle_{1I}. \quad (17)$$

Output-aligned current mode can be achieved using the following constraints:

1) output current is following I_{ref}; 2) real part of inductance current is equal to zero $\langle i_s(\tau)\rangle_{1R} = 0$; and (3) imaginary part of voltage is close to zero $\langle v_s(\tau)\rangle_{1I} \approx 0$ (due to small series resistance of LC-tank).

Therefore, during steady-state, it should satisfy equations derived using Eqs. (9), (13), (17):

$$\left\langle i_s(\tau)\right\rangle_{1I} = -\frac{\pi}{4} I_{ref}, \quad (18)$$

$$\frac{sind_1\pi}{\pi L_r} V_{in} - \frac{R_s}{L_r}\left\langle i_s(\tau)\right\rangle_{1R} - \frac{1}{L_r}\left\langle v_s(\tau)\right\rangle_{1R} + 2\pi f_s \left\langle i_s(\tau)\right\rangle_{1I} = 0, \quad (19)$$

$$\frac{1}{C_r}\left\langle i_s(\tau)\right\rangle_{1I} - 2\pi f_s \left\langle v_s(\tau)\right\rangle_{1R} = 0. \quad (20)$$

From these equations, the frequency can be found:

$$f_{s_{1,2}} = \frac{\left(-b \pm \sqrt{b^2 - 4ac}\right)}{2a}, \quad (21)$$

with coefficients,

$$\left.\begin{aligned} a &= I_{ref}\pi^3 \\ b &= -\frac{2V_{in}\sin d_1\pi}{L_r} \\ c &= -\frac{\pi I_{ref}}{4L_r C_r} \end{aligned}\right\} \quad (22)$$

3.2. SENSORLESS CURRENT CONTROL

The proposed current control diagram of the converter is illustrated in Fig. 3.

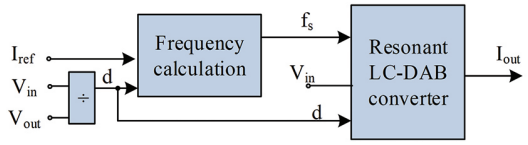

Fig. 3. Proposed current control diagram of the converter

The duty cycle is calculated by dividing the measured output voltage by the input voltage, as derived in (16). Switching frequency f_s is calculated by frequency calculation block, as described in (21), which is a function depending on the reference output current I_{ref} and the duty ratio d:

$$f_s = f\left(I_{ref}, d\right). \quad (23)$$

By processing these inputs, the resonant LC-DAB converter block, which utilizes the GAM calculation, determines output current, as described in (9)—(13):

$$X = f\left(w, d, V_{in}\right), \tag{24}$$

$$I_{out} = -\frac{4}{\pi} X(2), \tag{25}$$

Where,

$[(\langle i_s(\tau)\rangle_{1R} \langle i_s(\tau)\rangle_{1I} \langle v_0(\tau)\rangle_0 \langle v_s(\tau)\rangle_{1R} \langle v_s(\tau)\rangle_{1I})]^T$.

3.3. SMALL-SIGNAL MODEL

To design controllers and analyze stability for power converters, it is essential to obtain the small-signal control-to-output transfer function. This function shows the converter's dynamic response to small perturbations in the control signal.

The small signal model can be derived by perturbing the system in Eqs. (9)—(13) around steady-state values. The deviations of the state variables are expressed as follows:

$$\left.\begin{aligned} d &= D + \Delta d \\ i_{s1R} &= I_{s1R} + \Delta i_{s1R} \\ i_{s1I} &= i_{s1I} + \Delta i_{s1I} \\ v_o &= Vo + \Delta v_o \\ v_{s1R} &= v_{s1R} + \Delta v_{s1R} \\ v_{s1I} &= v_{s1I} + \Delta v_{s1I} \end{aligned}\right\}. \tag{26}$$

The variables in capital letter X denote the steady-state values, the large-signal states are defined by the variables in lowercase letters x and the perturbations are represented by the Δx variables.

Steady-state values can be derived by solving:

$$\frac{d}{dt}[\langle i_s(\tau)\rangle_{1R} \quad \langle i_s(\tau)\rangle_{1I} \quad \langle v_0(\tau)\rangle_0 \quad \langle v_s(\tau)\rangle_{1R} \quad \langle v_s(\tau)\rangle_{1I}]^T = 0. \tag{27}$$

Then, the small-signal model can be found by perturbation around steady-state value and have the form:

$$\Delta\dot{x} = A\Delta x + b\Delta I_{ref}, \tag{28}$$

$$\Delta\dot{v}_o = q\Delta x, \tag{29}$$

Where expressions of matrices are given in the Appendix A.1.

The control-to-output transfer function can be obtained using:

$$G_s(s) = \frac{\Delta v_0}{\Delta I_{ref}} = q\left[sI - A\right]^{-1} B. \tag{30}$$

3.4. VOLTAGE CONTROLLER DESIGN

A two-step controller can be implemented to address the issue of voltage regulation. The inner loop consists of a previously discussed current control loop, while the outer loop utilizes a PI controller, which is elaborated in this section. The analysis is performed using the small-signal method.

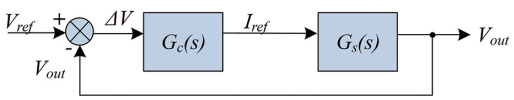

Fig. 4. Small signal closed-loop control diagram of the converter with PI controller

As depicted in Fig. 4, the PI controller is implemented between the GAM and frequency calculation block. $G_C(s)$ and $G_s(s)$ represents the transfer function of the controller and the converter, respectively. The measured output voltage V_{out} is subtracted from the desired output voltage V_{ref}. Then, the error signal is fed into a PI controller, which is implemented in closed-loop control.

The PI controller block determines the reference current as follows:

$$I_{ref} = K_p\left(V_{ref} - V_{out}\right) + K_i \int\left(V_{ref} - V_{out}\right)dt, \tag{31}$$

Where K_p and K_i are the proportional and integral coefficients of the PI controller, respectively.

The PI controller is used for voltage regulation. Combining the PI controller with an inner current loop reduces circulating reactive current during transients and provides alignment with secondary side voltage in most cases. The design and simulation results supporting these are presented in Section 5.

4. SIMULATION AND EXPERIMENTAL RESULTS

The converter with the proposed control has been implemented in MATLAB/Simulink. The main parameters used for converter simulation are given in Table 2. In the actual system, the input voltage is 400V, and the turn ratio n equals 3:1. However, for design simplicity, an input voltage of 30V and a turn ratio of 1:1 have been used.

Table 2. Simulation parameters

Parameter	Symbol	Value
Input voltage	V_{in}	35 V
Output voltage	V_{out}	20 V
Turn ratio	n	1:1
Resonant inductance	L_r	7.5 uF
Resonant capacitor	C_r	15 uF

4.1. EVALUATION OF SENSORLESS CURRENT CONTROL

Evaluating performance and sensitivity under voltage, circuit parameters, and reference current variations helps analyze the proposed model's effectiveness.

To compare how changes in output voltage impact output aligned current, waveforms on secondary side voltage and resonant current for different output voltages can be analyzed. V_{out} is set to be equal (15; 20; 25) V at I_{ref} = 50A. According to Fig. 5, it can be seen that the current is equal to zero at the beginning and the

end of each switching cycle when V_{out} =15V and 20V, ensuring ZVS and ZCS. When V_{out} =25V, the current has shifted due to the frequency approaching the resonant frequency, resulting in inaccuracies.

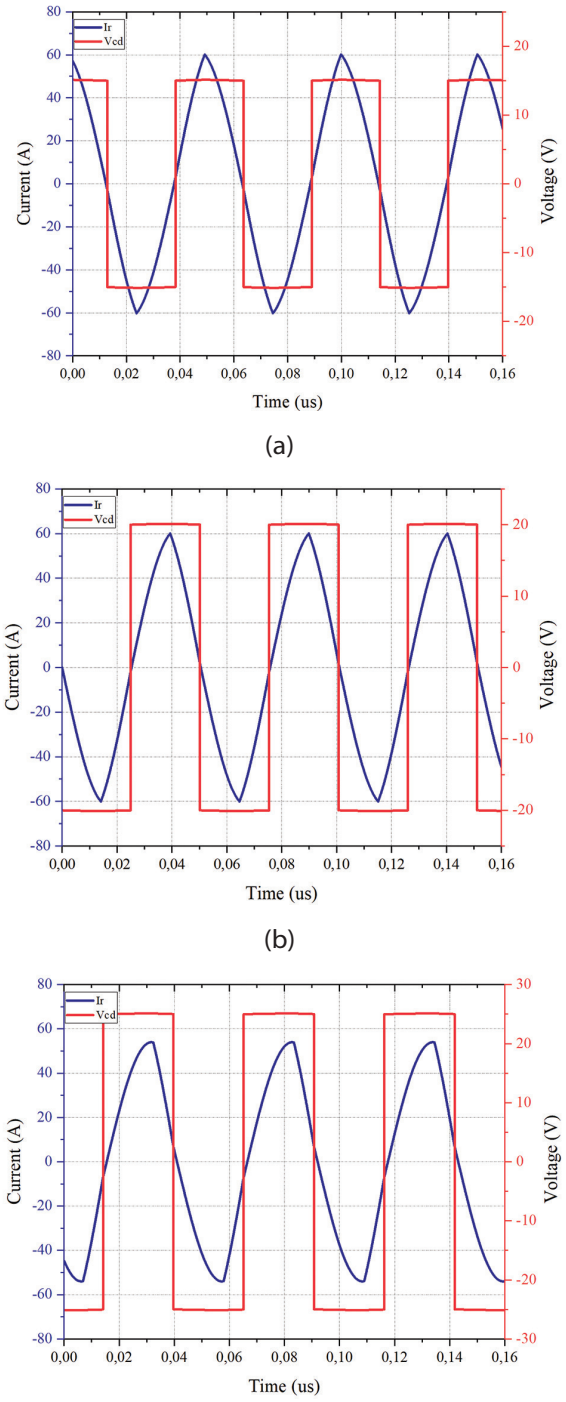

Fig. 5. Steady-state waveforms of the converter with proposed control technique @I_{ref} = 50A (a) V_{out} =15V (b) V_{out} =20V (c) V_{out} =25V

To demonstrate the dependence of alignment on parameter variation, the steady-state waveforms of the circuit when the resonant capacitor is adjusted to be 10% higher and 10% lower than the actual capacitance C_r at constant values of I_{ref} = 50A and V_{out} = 20V are obtained (Fig. 6). The results indicate that a 10% variation in capacitor value does not affect the ZVS and ZCS characteristics. Similarly, the steady-state waveforms when the resonant inductance is adjusted by 10% above and below the actual inductance L_r are also shown in Fig. 7. It demonstrates that change in inductance value results in a 2% variation in peak inductance current, with minimal effect on ZVS and ZCS characteristics.

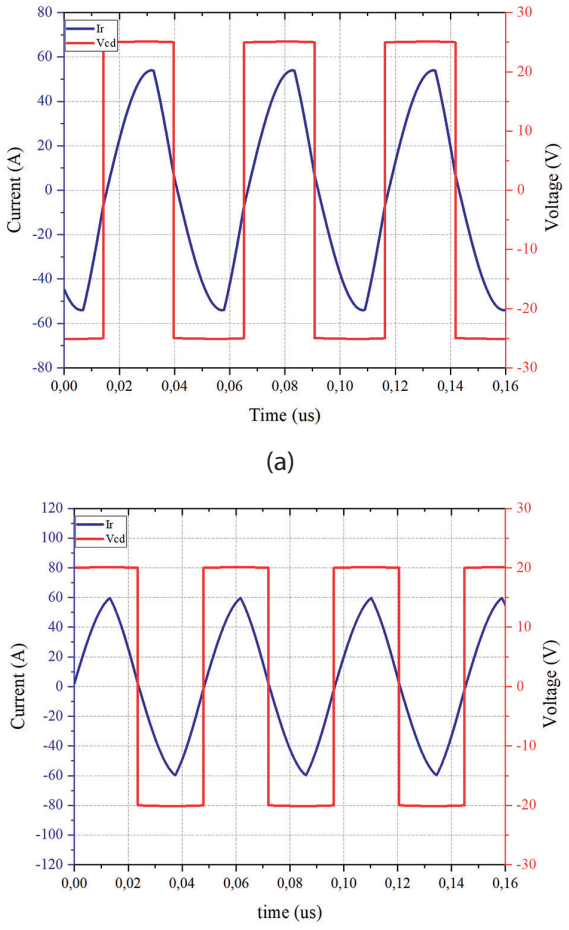

Fig. 6. Steady-state waveforms of the converter with proposed control technique @I_{ref} = 50A, V_{out} = 20V (a) 1.1 C_r (b) 0.9 C_r

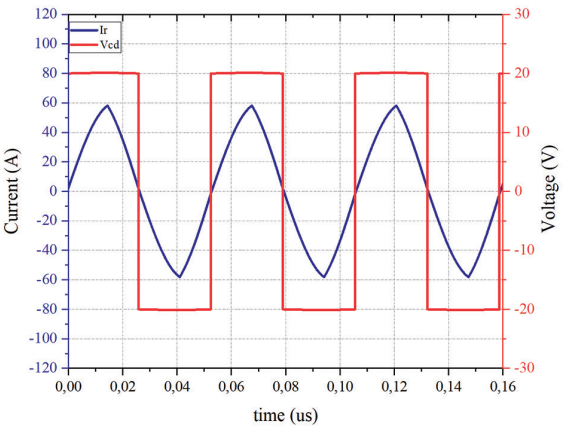

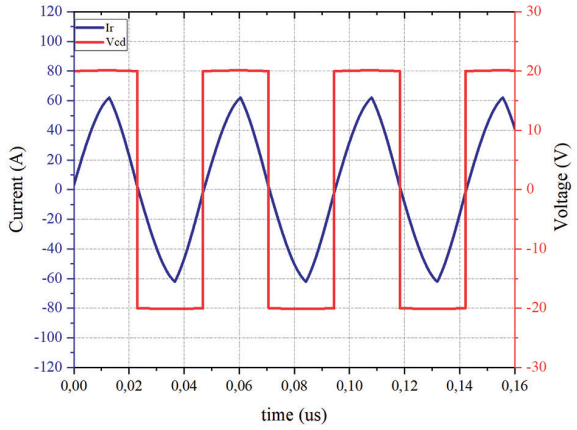

(b)

Fig. 7. Steady-state waveforms of the converter with proposed control technique @I_{ref} = 50A V_{out} =20V (a) 1.1 L_r (b) 0.9 L_r

Reference current perturbation may affect output current alignment with output voltage. When the current is leading, the output current is greater than zero. In contrast, when the current is lagging, the output will drop below zero. The frequency response of the current control loop has a bandwidth of approximately 4 kHz. To understand the circuit's behavior near this point, the reference current was perturbed with a sine signal of 4 kHz and an amplitude of 3 A. The steady-state response of the output current under these conditions is shown in Fig. 8. The perturbations cause the current to fall below zero at the zero crossing, indicating that the inductance current is lagging. In the worst case, the power factor is 0.97 and in the best case, it is 0.99. However, this difference may not be visible in the simulation waveforms due to the small angle between the voltage and current. To better demonstrate the efficiency of the proposed system, switching and conduction losses are calculated.

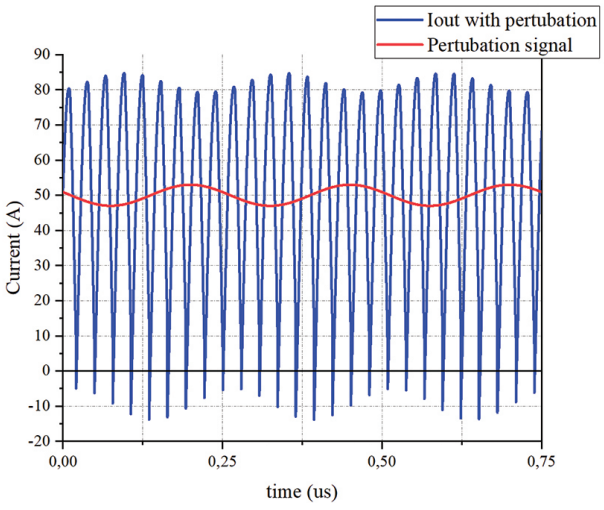

Fig. 8. Steady-state response of output current with reference current perturbation

$$P_{con} = I_{RMS}^2 \, \mathrm{R}_{\mathrm{dc,ON}} \tag{32}$$

ZVS switching occurs only on primary side lagging leg and its switching loss correspond to the internal capacitance C_{int}, current flowing during switching $I_{turn\text{-}off}$, switching frequency f_s, input voltage V_{in} and fall time t_{off}. Therefore, ZVS switching loss [33]:

$$P_{sw,ZVS} = C_{\mathrm{int}} f_s I_{turn-off} V_{in} t_{off} \tag{33}$$

ZCS switching losses occurs due to discharging of the parallel parasitic body capacitance of the transistors. It depends on internal capacitance C_{int}, switching frequency f_s, transistor voltages before turn-on which is equal to input voltage V_{in} for primary side losses and V_{out} for secondary side losses. Therefore, the loss during ZCS switching on primary side can be calculated as:

$$P_{sw,ZCS,pri} = \frac{1}{2} C_{\mathrm{int}} V_{in}^2 f_s \tag{34}$$

Similarly, the loss during ZCS switching on secondary side:

$$P_{sw,ZCS,\mathrm{sec}} = \frac{1}{2} C_{\mathrm{int}} V_{out}^2 f_s \tag{35}$$

Total switching losses for circuit includes 2 *ZVS* and 2 *ZCS* switching on primary side, and 2 *ZCS* switching on secondary side. Therefore, total switching losses:

$$P_{sw} = 2P_{sw,ZVS} + 2P_{sw,ZCS,pri} + 2P_{sw,ZCS,\mathrm{sec}} \tag{36}$$

These losses are calculated using parameters from the datasheets for both the primary side transistors INN100FQ025A [34] and secondary side transistors INN650TA030AH [35]. Fig. 9 illustrates the losses associated with the proposed strategy across various output currents while maintaining a steady output voltage of 20 V. The overall percentage of switching losses tends to be lower when the current is increased. Although higher current increases *ZVS* switching losses, it also leads to decreased switching frequency, which reduces both *ZVS* and *ZCS* switching losses. Additionally, conduction losses increase with current. Therefore, switching losses decrease with higher current. Overall, the losses remain below 8 W within the specified operational range, illustrating the efficient performance of the proposed modulation strategy across different operating conditions.

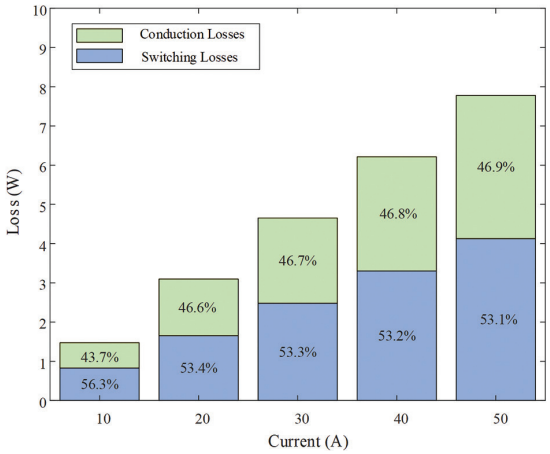

Fig. 9. Loss breakdown under output aligned current mode for different output current at output voltage of 20 V

4.2. EVALUATION OF CLOSED-LOOP VOLTAGE CONTROL

To evaluate outer loop voltage control, the frequency response characteristics of the current control loop with and without the outer loop can be analyzed. To achieve dynamic performance and stability, the gain and phase margins are set equal to 25 dB and 15°, respectively. Thus, using PI controller parameters from Table 2, the outer loop control satisfies targeted gain and phase margins, and it can be validated through the bode plot given in Fig. 10. Converter characteristics during a transient under load current step change of 10 A is shown in Fig. 11. Output current and voltage waveforms are smoothly adjusted to their new steady-state values.

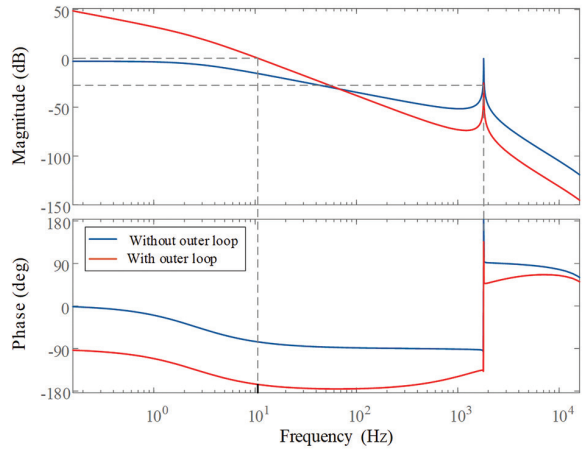

Fig. 10. Frequency response characteristics @ =50A without and with the outer loop

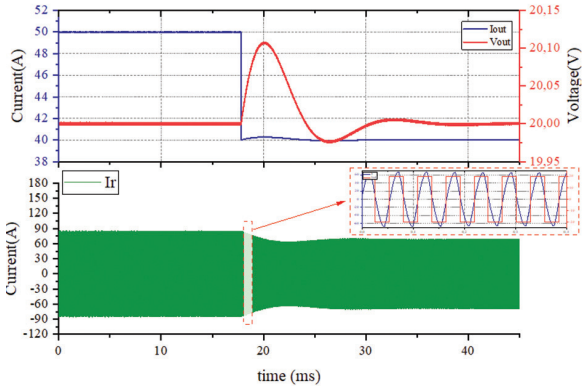

Fig. 11. Converter characteristics during transient under load current step change of 10A

Overall, analysis and simulation results represent that the proposed model provides current alignment with output voltage not only during steady-state but also during transients and parameter variation. The model performs satisfactorily even with frequency perturbations of up to approximately 4 kHz.

4.3. COMPARISON WITH EXISTING METHOD

A few papers have proposed a control technique for output-aligned current for resonant LC-DAB.

In this paper, the discrete-time technique has been implemented. This approach [8] is compared with the proposed method. This converter's parameters for open-loop modulation (phase shift ratio d and period T) can be determined using the reference output current I_{ref}, along with the input voltage V_{in}, and output voltage V_{out}, the resonant angle frequency ω_r. This method measures the resonant capacitor voltage over half of a sequence to facilitate accurate current calculations. The time t_2 is defined as half of the modulation period, while t_1 can be calculated using:

$$t_1 = \frac{-b \pm \sqrt{b^2 - 4ac}}{2a}, \tag{37}$$

With coefficients:

$$\begin{aligned} a &= \frac{-nV_{in}^2\omega_r^2}{C_r V_{out}\left(U_1 - U_2\right)} I_{ref}, \\ b &= -2U_1\omega_r^2, \\ c &= \frac{nV_{in}\pi^2}{2C_r\left(V_{in} - V_{out}\right)} I_{ref}. \end{aligned} \tag{38}$$

The duty cycle can be derived using (16), and the switching frequency can be derived as follows:

$$f = \frac{d}{2t_1}, \tag{39}$$

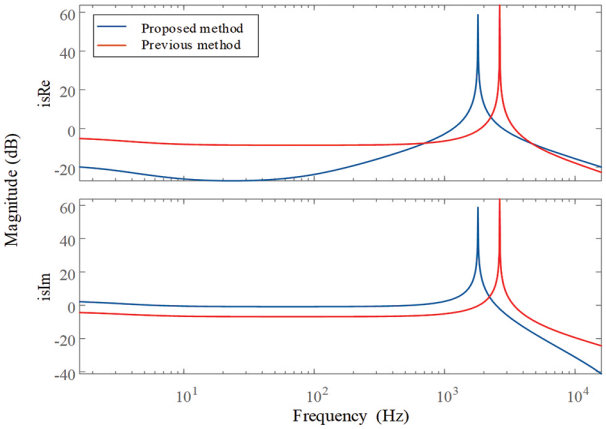

Fig. 12. Frequency response characteristics of real and imaginary parts of inductance current for two methods @I_{ref} =50A

Fig. 12 illustrates the frequency response of the real and imaginary parts of the inductor current using two methods. The existing model demonstrates a wider bandwidth range. However, the proposed method has better damping of the real part of the current over a wide range of frequencies, nearly up to 4 kHz. The proposed method has stable sensitivity close to the operating point, which minimizes the circulating output current even during transition. Fig. 13 shows the dependence of current on switching frequency between the previously established technique and the proposed method. The proposed model has lower switching frequencies for almost all current values, reducing switching and resistive losses.

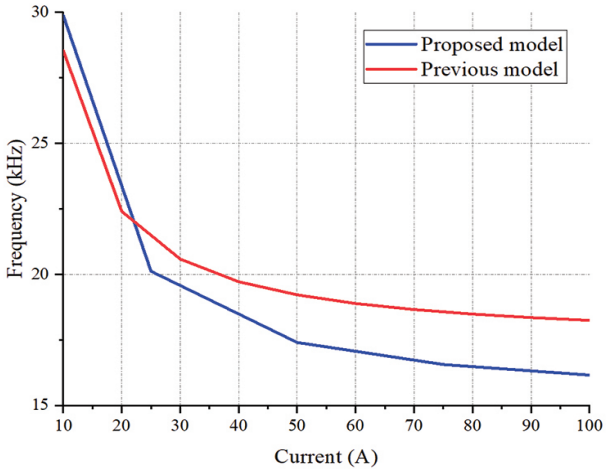

Fig. 13. Dependence of frequency on reference output current for two methods

In comparison with other works, the proposed technique has benefit of ability to work near resonant frequency which can further minimize switching losses. For instance, unified boundary control for resonant LC-DAB [26] can help to enhance converter efficiency by minimizing circulating current. However, it can work only at frequencies much higher than resonant frequency which may tend to higher switching losses. Another benefit of the proposed method is low cost and low complexity. In contrast, model with beat frequency dynamics [28] requires complex calculations to perform efficiently but has good performance in a wide frequency range. Moreover, the proposed model does not require the need of high frequency current measurement, as it is required by robust digital nonlinear controller [14]. While this controller can provide good dynamic performance with smooth transient response, it can only work with non-resonant DAB converter and requires high-frequency current measurement with complex calculations. As can be seen from extensive simulation, the proposed design also exhibits strong robustness, consistently maintaining current alignment with output voltage during steady-state conditions, transients, and parameter variations. In contrast, the accuracy of the method discussed in paper [21] relies on the model parameters, but it demonstrates good accuracy without the need for a PI-controller when the parameters are known.

Therefore, the proposed model is valuable for enhancing the dynamic performance of the resonant LC-DAB converter. It performs well under parameter variations, minimizes losses, effectively operates in the presence of a resonant circuit, and has low-cost with simple calculations.

4.4. EXPERIMENTAL RESULTS

The prototype of the LC-DAB was built and tested to demonstrate the effectiveness of the proposed model (fig. 14). The converter comprises four main components: the control PCB, the low-voltage side power PCB, the high-voltage side power PCB, and a high-frequency transformer. The prototype was built on a printed board by using GANFET (INN100FQ025A) on the input side and GANFET (INN650TA030AH) on the output side. The control PCB utilizes a DSP (TMS320F28374D) alongside an FPGA (EPM570T100I). These three PCBs are interconnected through connectors in a sandwich configuration to facilitate PWM signal transmission. Both the DC and AC sides feature pads for transformer connections, positioned between the power and control boards to optimize space and enable easy replacement and inspection of all PCBs.

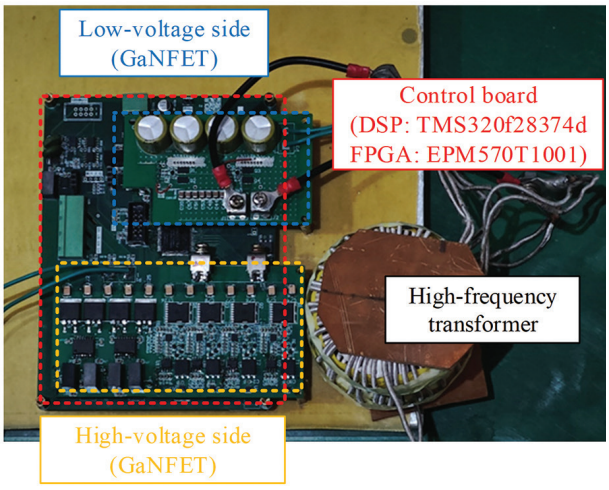

Fig. 14. Experimental setup

Fig. 15 depicts the experimental steady-state waveforms of primary and secondary side voltage and inductance current with proposed control technique at I_{ref}= 10A, V_{in}= 35V for output voltages V_{out}= 15V, V_{out}= 20V, V_{out}=30V. It represents alignment of output current with secondary side voltage even at frequencies near resonant. This shows the feasibility of proposed control technique.

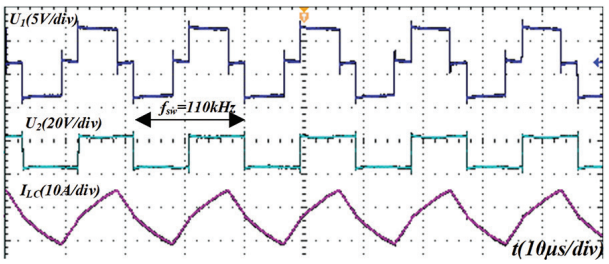

(a)

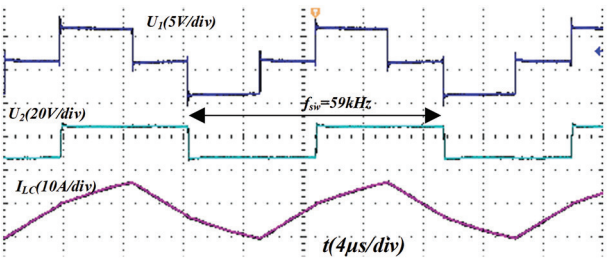

(b)

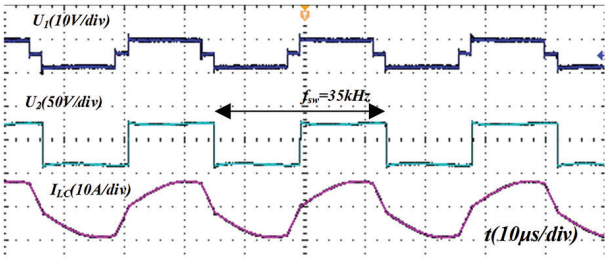

(c)

Fig. 15. Steady-state waveforms of the converter with proposed control technique @I_{ref} = 10A V_{in} = 35V (a) V_{out} =15V (b) V_{out}=20V (b) V_{out}=30V

5. CONCLUSION

This work presents a model for the resonant LC-DAB with output-aligned current. The GAM method represents the model of the converter in a continuous form, making analysis more straightforward. This model employs a two-stage control loop: an inner loop for current control and an outer loop utilizing a PI controller for voltage control. This approach helps to minimize circulating current during switching at the output side of the converter. Moreover, the analysis and design process for the proposed control strategy is discussed, and the corresponding simulation studies are conducted in the MATLAB/Simulink environment along with experimental results are presented in order to validate the effectiveness of this scheme. The obtained results show that not only the proposed method provides a promising solution for improving the dynamic performance of DAB converters, but it also helps to analyze the converter's behavior in output-aligned current mode.

6. APPENDIX

A. 1

The matrices A, B, q of small-signal model, derived in (28)-(29) are listed in the following.

$$A=\begin{bmatrix} -\frac{R_s}{L_r} & k_3+k_1^{'} & 0 & -\frac{1}{L_r} & 0 \\ -k_3-k_1 & -\frac{R_s}{L_r} & \frac{2}{\pi n L_r} & 0 & -\frac{1}{Lr} \\ 0 & -\frac{4}{C_{out}\, n\pi} & -\frac{1}{C_{out}\, R_{out}} & 0 & 0 \\ \frac{1}{C_r} & 0 & 0 & 0 & k_3+k_1 \\ 0 & \frac{1}{C_r} & 0 & -k_3-k_1 & 0 \end{bmatrix};$$

$$B=\begin{bmatrix} -i_{s_{Im}}\, k_1 - i_{s_{Im}}\, k_2 \\ i_{s_{Re}}\, k_1 + i_{s_{Re}}\, k_2 \\ 0 \\ -v_{s_{Im}}\, k_1 - v_{s_{Im}}\, k_2 \\ v_{s_{Re}}\, k_1 + v_{s_{Re}}\, k_2 \end{bmatrix};$$

q=[(0 0 1 0 0)];

With coefficients:

$$k_1=\frac{2\mathrm{U}_1 \sin\left(\frac{\pi \mathrm{U}_2}{\mathrm{U}_1}\right)}{\pi^2 \mathrm{I}_{ref}^2 \mathrm{L}_r};$$

$$k_2=\frac{4U_1^2 \sin\left(\frac{\pi \mathrm{U}_2}{\mathrm{U}_1}\right)^2}{\pi^4 \mathrm{I}_{ref}^3 \mathrm{L}_r^2 \sqrt{\frac{1}{\mathrm{C}_r \mathrm{L}_r}+\frac{4U_1^2 \sin\left(\frac{\pi \mathrm{U}_2}{\mathrm{U}_1}\right)^2}{\pi^4 \mathrm{I}_{ref}^2 \mathrm{L}_r^2}}};$$

$$k_3=\sqrt{\frac{1}{C_r L_r}+\frac{4U_1^2 \sin\left(\frac{\pi U_2}{U_1}\right)^2}{\pi^4 I_{ref}^2 L_r^2}}.$$

7. REFERENCES

[1] F. Krismer, J. W. Kolar, "Accurate power loss model derivation of a high-current dual active bridge converter for an automotive application", IEEE Transactions on Industrial Electronics, Vol. 57, No. 3, 2010, pp. 881-891.

[2] Y. Shi, R. Li, Y. Xue, H. Li, "Optimized operation of current-fed dual active bridge DC-DC converter for PV applications", IEEE Transactions on Industrial Electronics, Vol. 62, No. 11, 2015, pp. 6986-6995.

[3] W. R. L. Garcia, P. Tixador, B. Raison, A. Bertinato, B. Luscan, C. Creusot, "Technical and economic analysis of the R-type SFCL for HVDC grids protection", IEEE Transactions on Applied Superconductivity, Vol. 27, No. 7, 2017, pp. 1-9.

[4] A. Nisar, M. S. Thomas, "Comprehensive control for microgrid autonomous operation with demand response", IEEE Transactions on Smart Grid, Vol. 8, No. 5, 2017, pp. 2081-2089.

[5] L. Zhuolan, Z. Yu, Z. Mengyuan, "Model and Control for Transient Process of Dual-Bridge Series Resonant Converter", IEEE Transactions on Power Electronics, Vol. 39, No. 8, 2024, pp. 9202-9220.

[6] M. Sato, Y. Tada, M. Uno, "Multi-Port Converter Integrating Automatic Current Balancing Interleaved PWM Converter and Dual Active Bridge Converter with Improved Transformer Utilization", Proceedings of IECON 2020 - The 46th Annual Conference of the IEEE Industrial Electronics Society, Singapore, 18-21 October 2020, pp. 1377-1382.

[7] X. Li, J. Huang, Y. Ma, X. Wang, J. Yang, X. Wu, "Unified modeling, analysis, and design of isolated bi-

directional CLLC resonant DC-DC converters", IEEE Journal of Emerging and Selected Topics in Power Electronics, Vol. 10, No. 2, 2022, pp. 2305-2318.

[8] G. Chen, N. Xu, L. Yuan, M. Humayun, M. M. Khan, "A DC-DC Center-Tapped Resonant Dual-Active Bridge with Two Modulation Techniques", Electronics, Vol. 9, No. 10, 2020, p. 1699.

[9] S. M. S. I. Shakib, S. Mekhilef, "A Frequency Adaptive Phase Shift Modulation Control Based LLC Series Resonant Converter for Wide Input Voltage Applications", IEEE Transactions on Power Electronics, Vol. 32, No. 11, 2017, pp. 8360-8370.

[10] P. Qu, Z. Li, P. Wang, Y. Li, "An improved analysis considering harmonic components for high-frequency isolated dual-active-bridge series resonant DC-DC converter", Proceedings of the Transportation Electrification Asia-Pacific, Beijing, China, 31 August - 3 September 2014, pp. 1-4.

[11] E. Babaie, M. E. S. Mahmoodieh, M. Sabahi, "Investigating buck dc-dc converter operation in different operational modes and obtaining the minimum output voltage ripple considering filter size", Journal of Power Electronics, Vol. 11, No. 6, 2011, pp. 793-800.

[12] E. Babaie, M. E. Seyed Mahmoodieh, H. M. Mahery, "Operational modes and output voltage ripple analysis and design considerations of buck-boost dc-dc converters", IEEE Transactions on Industrial Electronics, Vol. 59, No. 1, 2012, pp. 381-391.

[13] S. P. Engel, N. Soltau, H. Stagge, R. W. De Doncker, "Dynamic and balanced control of three-phase high-power dual-active bridge DC-DC converters in DC-grid applications", IEEE Transactions on Power Electronics, Vol. 28, No. 4, 2013, pp. 1880-1889.

[14] I. Askariyan, S. Bagawade, M. Pahlevani, A. M. Knight, A. Bakhshai, "Robust Digital Nonlinear Control System for Dual Active Bridge (DAB) DC/DC Converters With Asymmetric Half-Cycle Modulation", IEEE Journal Of Emerging And Selected Topics In Industrial Electronic, Vol. 1, No. 2, 2020, pp. 123-132.

[15] S. Dutta, S. Bhattacharya, M. Chandorkar, "A novel predictive phase shift controller for bidirectional isolated DC to DC converter for high power applications", Proceedings of the IEEE 30th International Symposium on Industrial Electronics, Raleigh, NC, USA, 15-20 September 2012, pp. 418-423.

[16] S. Dutta, S. Hazra, S. Bhattacharya, "A digital predictive current-mode controller for a single-phase high-frequency transformer-isolated dual-active bridge DC-to-DC converter", IEEE Transactions on Industrial Electronics, Vol. 63, No. 9, 2016, pp. 5943-5952.

[17] S. Wei, Z. Zhao, K. Li, L. Yuan, W. Wen, "Deadbeat current controller for bidirectional dual-active-bridge converter using an enhanced SPS modulation method", IEEE Transactions on Power Electronics, Vol. 36, No. 2, 2021, pp. 1274-1279.

[18] M. Nasr, S. Poshtkouhi, N. Radimov, C. Cojocaru, O. Trescases, "Fast average current mode control of dual-active-bridge DC-DC converter using cycle-by-cycle sensing and self-calibrated digital feedforward", Proceedings of the IEEE Applied Power Electronics Conference and Exposition, Tampa, FL, USA, 26-30 March 2017, pp. 1129-1133.

[19] N. Hou, Y. Zhang, Y. W. Li, "A Load-Current-Estimating Scheme with Delay Compensation for the Dual-Active-Bridge DC-DC Converter", IEEE Transactions on Power Electronics, Vol. 37, No. 3, 2022, pp. 2636-2647.

[20] Y. Deng, W. Song, S. Yin, M. Zhong, K. Yang, X. Feng, "A Model Predictive Control Scheme without Current Sensor of Dual Active Bridge DC-DC Converters: Improving Dynamic Performance and Reducing Hardware Cost", IEEE Transactions on Transportation Electrification, Vol. 9, No. 2, 2022, pp. 2916-2928.

[21] T. Q. Duong, S. J. Choi, "Sensor-Reduction Control for Dual Active Bridge Converter Under Dual-Phase-Shift Modulation", IEEE Access, Vol. 10, 2022, pp. 63020-63033.

[22] L. Zhu, "A novel soft-commutating isolated boost full-bridge ZVS-PWM DC-DC converter for bidirectional high power applications", Proceedings of the IEEE 35th Annual Power Electronics Specialists Conference, Aachen, Germany, 20-25 June 2004, pp. 2141-2146.

[23] R. Twiname, W. Malan, J. Minogue, D. J. Thrimawithana, U. K. Madawala, C. Baguley, "A novel

dual active bridge topology with a tuned CLC network", Proceedings of the IEEE International Conference on Industrial Technology, Busan, South Korea, 26 February - 1 March 2014, pp. 895-900.

[24] L. Rossetto, G. Spiazzi, "Series resonant converter with wide load range", Proceedings of the IEEE Industry Applications Conference Thirty-Third IAS Annual Meeting, St. Louis, MO, USA, 12-15 October 1998, pp. 1326-1331.

[25] D. Czarkowski, M. K. Kazimierczuk, "Phase-controlled series-parallel resonant converter", IEEE Transactions on Power Electronics, Vol. 8, No. 3, 1993, pp. 309-319.

[26] G. Chen, X. Li, S. Zhou, "Unified Boundary Control with Phase Shift Compensation for Dual Bridge Series Resonant DC-DC Converter", IEEE Access, Vol. 8, 2020, pp. 131137-131149.

[27] D. J. Linton, C. A. Teixeira, R. H. Wilkinson, B. P. McGrath, D. G. Holmes, J. Riedel, "Adaptive modulation of resonant DAB converters for wide range ZVS operation with minimum reactive circulating power", IEEE Transactions on Industry Applications, Vol. 58, No. 6, 2022, pp. 7396-7407.

[28] S. Chakraborty, K. Hatua, "Modeling with beat frequency dynamics and phase-frequency control design for a dual-bridge series resonant converter", IEEE Transactions on Power Electronics, Vol. 69, No. 8, 2022, pp. 7952-7962.

[29] T. Chen, R. Yu, A. Q. Huang, "A bidirectional isolated dual-phase-shift variable-frequency series resonant dual-active-bridge GaN AC-DC converter", IEEE Transactions on Industrial Electronics, Vol. 70, No. 4, 2023, pp. 3315-3325.

[30] H. Qin, J. W. Kimball, "Generalized Average Modeling of Dual Active Bridge DC–DC Converter", IEEE Transactions on Power Electronics, Vol. 27, No. 4, 2012, pp. 2078-2084.

[31] A. K Dubey, N. Lakshminarasamma, "Modeling of series resonant dual active bridge converter for dc microgrid application", Proceedings of the IEEE International Conference on Environment and Electrical Engineering and IEEE Industrial and Commercial Power Systems, Prague, Czech Republic, 28 June - 1 July 2022, pp. 1-6.

[32] K. Takagi, H. Fujita, "Dynamic control and performance of a dual-active-bridge DC-DC converter", IEEE Transactions on Power Electronics, Vol. 33, No. 9, 2017, pp. 7858-7866.

[33] R. Zhang, M.M. Khan, J. Zhao, A. Mukhametdinova, M. Q. Khan, "A Four-Degrees-of-Freedom Modulation Strategy for Series Resonant DAB DC-AC Application", International Journal of Circuit Theory and Applications, 2024. (in press)

[34] Innoscience, "100V GaN Enhancement-mode Power Transistor", INN100FQ025A datasheet, https://www.innoscience.com/site/product_details/479 (accessed: 2025)

[35] Innoscience, "650V GaN Enhancement-mode Power Transistor", INN650TA030AH datasheet, https://www.innoscience.com/site/product_details/830 (accessed: 2025)